

# Less Is More 🍊: Scalable Visual Navigation from Limited Data

Yves Inglin<sup>1</sup> Jonas Frey<sup>2,3</sup> Changan Chen<sup>1</sup> Marco Hutter<sup>1</sup>

<sup>1</sup>ETH Zurich <sup>2</sup>Stanford University <sup>3</sup>UC Berkeley

**Abstract**—Imitation learning provides a powerful framework for goal-conditioned visual navigation in mobile robots, enabling obstacle avoidance while respecting human preferences and social norms. However, its effectiveness depends critically on the quality and diversity of training data. In this work, we show how classical geometric planners can be leveraged to generate synthetic trajectories that complement costly human demonstrations. We train *Less is More* (LiMO), a transformer-based visual navigation policy that predicts goal-conditioned SE(2) trajectories from a single RGB observation, and find that augmenting limited expert demonstrations with planner-generated supervision yields substantial performance gains. Through ablations and complementary qualitative and quantitative analyses, we characterize how dataset scale and diversity affect planning performance. We demonstrate real-robot deployment and argue that robust visual navigation is enabled not by simply collecting more demonstrations, but by strategically curating diverse, high-quality datasets. Our results suggest that scalable, embodiment-specific geometric supervision is a practical path toward data-efficient visual navigation.

## I. INTRODUCTION

Navigation on mobile robots has traditionally followed a geometric pipeline: build a map, estimate traversability, and plan a path to the goal. While principled and precise for collision avoidance, this approach struggles when semantic understanding or nuanced behaviors are required. Purely geometric reasoning treats bushes or tall grass as rigid obstacles, yet it can misjudge glare, puddles, or loose gravel as safe. Encoding social norms and complex preferences is likewise difficult in unstructured, real-world settings.

Current work focuses on learning navigation behaviors directly from RGB images using imitation learning, with an emphasis on scaling up both model capacity and dataset size by training on data from different embodiments. The resulting class of models, termed foundation navigation models, has shown promising preliminary results, demonstrating multi-embodiment control and goal-conditioned navigation via poses, images, or language.

Scaling-first approaches have proven particularly effective in autonomous driving, where virtually unlimited human demonstration data can be collected. However, in many real-world robotic settings, data is scarce, necessitating the incorporation of more first-principled approaches into the training of navigation policies. In such settings, transparent and rigorous analysis of model limitations becomes essential for guiding future development. Under this lens, we identify five core limitations that can pose significant challenges for current visual navigation models:

(i) The navigation capability relies on costly real-world expert demonstrations. (ii) Action diversity in existing datasets

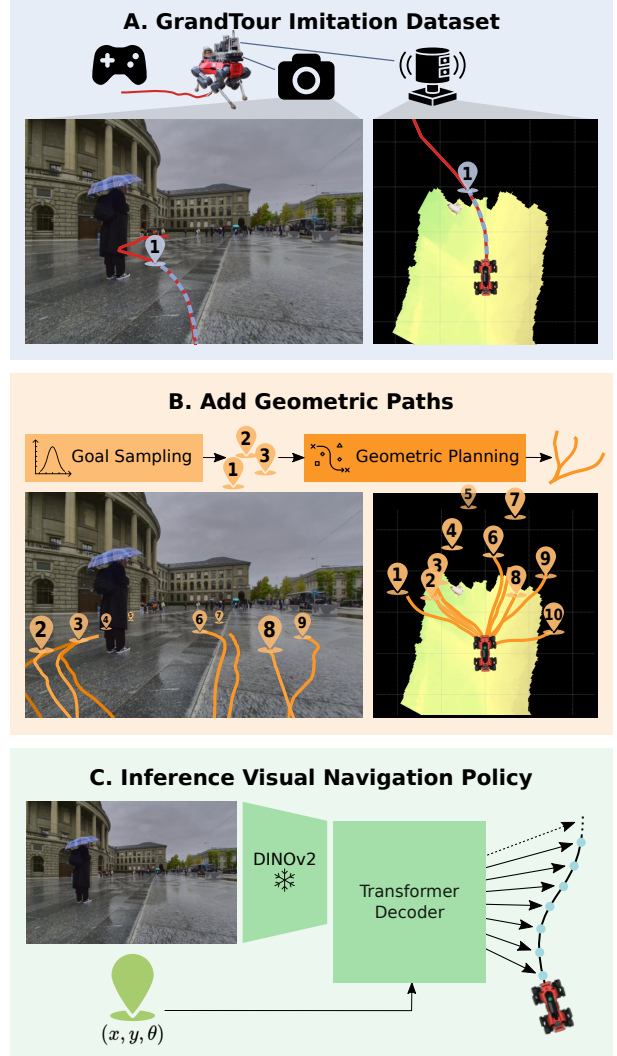


Fig. 1. Starting from GrandTour [1], a high-quality dataset of recorded quadruped robot missions, we augment the limited real-world expert demonstrations with planner-generated trajectories to scale supervision for imitation learning. The augmented dataset is then used to train LiMO, an end-to-end visual navigation policy.

is limited, biasing navigation toward simple, conservative motion. (iii) Models must learn geometric obstacle avoidance entirely from demonstrations. (iv) Current models trained on cross-embodiment data cannot choose actions that are desirable for a specific embodiment. (v) Training often focuses only on feasible goals. In response, we ask: How can we build upon the promising imitation learning framework while efficiently supervising navigation policies at scale to acquire

both semantic understanding and robust navigation behavior, conditioned on the embodiment?

We propose LiMO, an *embodied visual navigation* policy that, given a single RGB image and an SE(2) goal, predicts a sequence of waypoints for local goal-conditioned navigation. To enable scalable supervision, we introduce two complementary datasets derived from GrandTour [1]. The *teleop* dataset transfers semantic preferences from expert trajectories, while the *geometric* dataset scales supervision by sampling goals and labeling them with planner-generated trajectories. Because sampled goals may be infeasible, LiMO also learns safe exploratory behavior and robustness to unreachable targets, making it a practical drop-in vision-based local planner.

Across held-out GrandTour missions, LiMO trained on the *augmented* dataset (teleop + geometric) achieves substantially higher *Success weighted by (normalized inverse) Path Length*(SPL) [2] than when trained solely on teleop-data, while preserving strong performance on teleop-style splits. We show that the policy adapts paths to visible structures and selects semantically reasonable shortcuts when safe, while transparently exposing the approach’s current limitations. We further demonstrate real-robot deployment, illustrating LiMO’s practicality as a drop-in replacement for local path planning. We release all datasets and pretrained models to enable reproducibility and further research.

#### Contributions.

- LiMO: end-to-end, embodied, goal-conditioned navigation from a single RGB image
- A scalable imitation learning pipeline combining expert demonstrations and planner-generated supervision
- Analysis linking path-planning performance to action diversity
- Closed-loop real-robot deployments of LiMO as a drop-in local planner

## II. RELATED WORK

### A. Geometric Path Planning

Existing geometric planners either use raw sensory data directly or rely on aggregated spatiotemporal geometric information, such as elevation maps, to compute feasible and safe paths [3]. These planners typically frame path planning as a search or optimization problem. Prominent approaches include graph-based search algorithms [4] and optimization methods minimizing a cost function, such as MPPI [5] or iCEM [6].

These methods are interpretable and allow easy behavior tuning by adjusting the cost function, e.g., to increase clearance to obstacles or change velocity profiles. This, together with formal guarantees of convergence to an optimal path (if it exists), makes them a favored option in industry. However, purely geometric sensing can miss semantically salient cues in unstructured terrain; e.g., unstable materials may appear traversable, while light grass is interpreted as a hard obstacle, missing nuanced navigation behavior. This motivates the use of vision to incorporate semantic understanding into robot navigation [7], [8].

### B. Visual Navigation

Visual navigation aims to learn navigation behaviors directly from camera input. Previous works leverage reinforcement learning [9], [10] and imitation learning (IL) [11], [12] to train visuomotor control policies from raw images.

IL has produced remarkable advances in autonomous driving (AD) [13]–[16]. Lately, several large-scale, high-quality AD datasets have been made available [17]–[19]. The use of IL for navigating other types of mobile robots is hindered by the limited availability of demonstration data. Collecting expert demonstrations is costly, and existing datasets typically cover only a few hours of operation, which limits robustness and generalization.

Recent goal-image-conditioned models, such as ViNT [20], use transformer-based architectures to learn navigation policies intended to generalize across varied settings and robot embodiments. NoMaD [21] extends ViNT by incorporating a diffusion head for trajectory prediction, which supports goal-conditioned navigation and unconditioned exploration. FlowNav [22] is based on NoMaD but replaces diffusion with conditional flow matching (CFM) to improve inference efficiency. Additionally, FlowNav uses an off-the-shelf monocular depth estimation model to generate depth priors, which are then fed to the model. These models use a goal image (the observation when the robot is at the goal) for goal-conditioning. This goal image is available during training on pre-recorded robot demonstrations, but it may not be available during deployment.

To overcome the limited data problem, [20]–[22] train on a mix of datasets; however, the overall scale remains limited. The total hours reported for ViNT/NoMaD training are 80 h across the collected datasets (see Tab I) and even less for FlowNav, which is modest given the complexity of the task. These works compellingly demonstrate the promise of IL for navigation; nevertheless, the scarcity of expert data continues to hinder generalization.

Also notable is the significant diversity of embodiments in the training data, ranging from slow differential-drive robots operating at 0.5 m/s to fast all-terrain vehicles reaching 20 m/s. To handle this variation, the models are provided with the past five camera frames to implicitly capture embodiment, and they rely on a normalized action space where predicted waypoints are scaled by each robot’s maximum speed.

However, it is questionable whether cross-embodiment training genuinely improves model performance or whether it is primarily a compromise to increase dataset size. In many cases, training navigation models on embodiment-specific data may be preferable, enabling the full use of a given platform’s motion capabilities. For instance, when training on wheeled-robot data, a quadruped robot might learn overly conservative behaviors, such as avoiding stairs, thereby unnecessarily limiting its mobility and failing to leverage its full potential.

LiReN [37] approaches data scarcity by continuously improving the model during deployment. They first use offline RL to train a navigation policy on the same multi-embodiment dataset as ViNT. Then they deploy the model and use an

TABLE I  
OVERVIEW OF DATASETS FOR IMITATION LEARNING

Dataset	Platform	Total [h]	Env.	Sup.
<b>Expert (ViNT &amp; NoMaD)</b>				
BDD [17]	Cars	10	R	H
Berkeley [23]	Jackal	4	S	H
CoryHall [24]	RC car	2	H	H
GoStanford [25]	TurtleBot2	17	O	H
NeBula [26]	ATV	10	F	H
RECON [27]	Jackal	25	F	H
SACSoN [28]	TurtleBot2	75	O	H
SCAND-J [29]	Jackal	1	W	H
SCAND-S [29]	Spot	8	W	H
Seattle [30]	Warthog	1	F	H
TartanDrive [31]	ATV	7	F	H
<b>Others</b>				
LeLaN [32]	Humans+Robots	129	D	O
CityWalker [33]	Humans+Cars	2000	C	O
FrodoBots-2k [34]	Earth Rover Zero	2000	U	O
FrodoBots-2k(f) [34]	Earth Rover Zero	700	U	O
OmniVLA [35]	Cars+Humans+Robots	9500	D	O
TartanGround [36]	Robots	40	D	P
<b>Ours</b>				
GrandTour [1]	ANYmal D	6	D	H
Ours	ANYmal D	2162	D	P

**Env. legend:** R=on-road, S=suburban, H=hallways, O=office, F=off-road, W=sidewalks, C=city walking/driving, U=urban sidewalks/ped. zones, D=highly diverse (in/out).

**Sup.:** H=Human Expert, P=Geometric Planner, O=Other.

actor-critic algorithm to continuously improve it during deployment without needing a human expert to collect more data. LeLaN [32] uses NoMaD and a vision–language model (VLM) to automatically label first-person view (FPV) YouTube videos for navigation policy learning.

CityWalker [33] also uses a dataset of FPV videos from YouTube, on which it runs visual odometry (VO) to automatically generate supervision. The FrodoBots-2k dataset [34] uses crowdsourcing; volunteers remotely drive inexpensive robots (e.g., Earth Rover Zero) to collect demonstrations in urban pedestrian zones. This strategy scales data collection without on-site experts; however, the dataset suffers from poor tracking, inaccurate localization, and low-quality sensors. This is addressed by using Model-Based ReAnnotation (MBRA) [34], an approach that transforms a low-quality dataset into a filtered version with high-quality supervision.

NaVILA [38] scales instruction-following navigation using human egocentric touring videos from YouTube. They estimate camera motion using an off-the-shelf model, generate language descriptions of the tours using a VLM, and train a two-stage vision–language navigation model on the resulting data.

OmniVLA [35] is an omni-modal vision-language-action (VLA) model for navigation that supports goal conditioning via 2D goal poses, egocentric goal images, natural language instructions, and their combinations. Built on top of OpenVLA [39], OmniVLA leverages a large pretrained VLA backbone and is further trained on approximately 9500 h of navigation data. This dataset is the combination of [20], [21], [32], [34], [40] datasets from 10 different robotic platforms.

Notably, the dataset mixture is heavily skewed towards BDD-V, i.e., on-road autonomous driving data. They use a customized MBRA-style [34] approach to generate synthetic, feasible supervision for their target robots on BDD-V.

Instead of predicting waypoints directly, VENTURA [41] uses an internet-pretrained image diffusion model to generate an image-space path mask conditioned on the current RGB observation and a language instruction. Another model then converts the image-based path mask into waypoints. To scale supervision without manual annotations or accurate odometry, VENTURA generates path-mask labels indicating where the robot moved during deployment from egocentric videos using point tracking and adds captions using a VLM.

While [32], [35], [38], [41] study language-conditioned navigation, we focus only on goal-conditioned visual navigation. Despite strong progress in visuomotor policies, geometric reasoning in cluttered environments remains challenging, likely reflecting the limited geometric diversity of current datasets, which are often dominated by AD or conservative motion.

LoGoPlanner [42] addresses this by grounding navigation in metric-scale geometry through auxiliary localization and reconstruction tasks. In contrast, we scale embodiment-specific geometric supervision by augmenting a high-quality legged-robot dataset with planner-generated trajectories, achieving geometry-aware performance without explicit 3D reconstruction at deployment. Our work extends the GrandTour [1] dataset’s 6 h of deployments to thousands of hours of diverse, high-quality, embodiment-specific trajectories.

### III. METHOD

#### A. Overview

Given an RGB image  $\mathbf{I}$  and a goal pose  $\mathbf{g} = [x, y, \theta] \in \text{SE}(2)$  in the robot-centric frame, the objective is to predict a path  $\mathbf{s}_{1:N}$  of  $N$  waypoints  $\mathbf{s}_i = [x_i, y_i, \theta_i] \in \text{SE}(2)$  that safely guides the robot towards the goal. We address this by training a policy  $\pi : (\mathbf{I}, \mathbf{g}) \mapsto \mathbf{s}_{1:N}$  via IL, which we call LiMO.

From a base dataset  $\mathcal{D}_{\text{Base}}$  containing time-synchronized RGB video and elevation maps from expert teleoperated deployments, we extract front-camera images paired with executed  $\text{SE}(2)$  path segments to form the *teleop* dataset  $\mathcal{D}_{\text{TEL}}$  (Sec. III-C1). We then sample additional goals per frame and label them with trajectories planned using a geometric MPPI planner (Secs. III-B and III-C2), yielding the *geometric* dataset  $\mathcal{D}_{\text{GEO}}$ . Finally, we train LiMO on the augmented dataset  $\mathcal{D}_{\text{AUG}} = \mathcal{D}_{\text{TEL}} \cup \mathcal{D}_{\text{GEO}}$  (Sec. III-D).

#### B. MPPI Planning

MPPI is a gradient-free optimization algorithm used for robot motion and path planning. Originally introduced in [5], MPPI’s effectiveness has been demonstrated in several real-world experiments, such as high-speed driving and whole-body control of legged robots [5], [43]. We use MPPI to solve the following optimization problem:

$$\min_{\mathbf{a}_{1:N}} J(\mathbf{s}_1, \mathbf{a}_{1:N}), \quad (1)$$

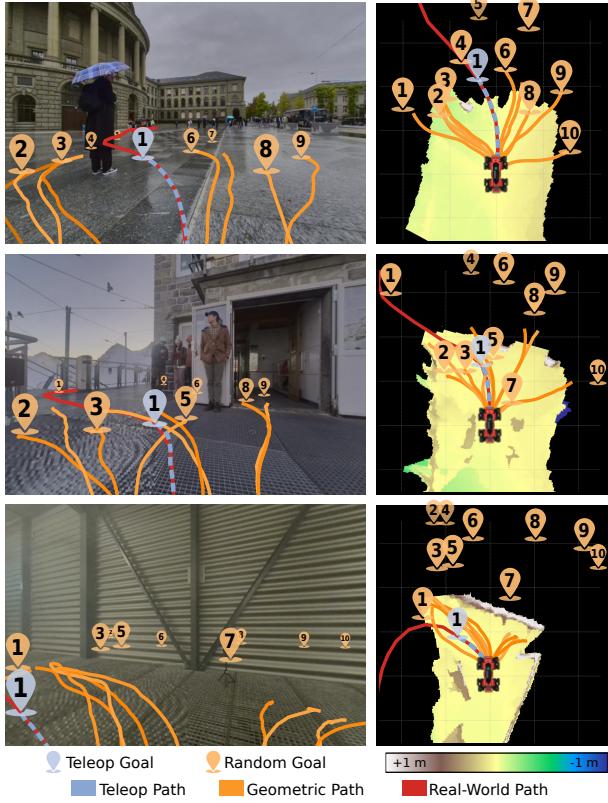


Fig. 2. Three representative samples from the augmented dataset  $\mathcal{D}_{\text{AUG}}$ . Each row shows the front camera image (left) and the corresponding elevation map (right). Teleoperated, geometric, and real-world paths are overlaid with their associated goals.

where  $\mathbf{a}_{1:N}$  is a sequence of command velocities  $\mathbf{a}_i = [v_i^x, v_i^y, \omega_i]$ , with  $v_i^x, v_i^y, \omega_i$  representing the linear and angular velocities, respectively, and  $J : (\mathbf{s}_1, \mathbf{a}_{1:N}) \mapsto c \in \mathbb{R}$  denoting a predefined cost function that encourages goal-reaching and safety, conditioned on the current state  $\mathbf{s}_1 \in \text{SE}(2)$ .

MPPI solves the optimization by iteratively sampling a population of command velocity sequences  $\mathbf{a}_{1:N}$ . It then uses  $J$  to weight the population members and update the population distribution, preferring low-cost members.

The future states are computed based on the current state  $\mathbf{s}_1$  and a dynamics model  $\mathbf{s}_{i+1} = f(\mathbf{s}_i, \mathbf{a}_i)$ . The dynamics model  $f$  can be learned or classically derived. In our case, we use a simple piecewise-constant velocity kinematic model in  $\text{SE}(2)$ :

$$\theta_{i+1} = \theta_i + \omega_i \Delta t, \quad (2)$$

$$\begin{bmatrix} x_{i+1} \\ y_{i+1} \end{bmatrix} = \begin{bmatrix} x_i \\ y_i \end{bmatrix} + \mathbf{R}(\theta_i) \begin{bmatrix} v_x^i \\ v_y^i \end{bmatrix} \Delta t, \quad (3)$$

where  $\mathbf{R}(\theta_i) \in \text{SO}(2)$  is the planar rotation matrix that maps body-frame velocities to the world frame and  $\Delta t$  is the control timestep.

To encourage goal reaching while ensuring robot safety, we construct the cost function as follows:

$$\begin{aligned} J(\mathbf{s}_1, \mathbf{a}_{1:N}) = & w_{\text{trav}} C_{\text{trav}}(\mathbf{s}_{1:N}) + w_{\text{goal}} C_{\text{goal}}(\mathbf{s}_{1:N}) \\ & + w_{\text{effort}} C_{\text{effort}}(\mathbf{a}_{1:N}). \end{aligned} \quad (4)$$

1) *Traversability Cost ( $C_{\text{trav}}$ )*: A convolutional neural network (CNN) [44], [45] is used to compute a traversability map  $\mathbf{T}$  from the elevation map  $\mathbf{E}$ . The CNN is trained to provide an embodiment-specific traversability estimate based on the robot's capabilities. The traversability cost is the sum of the grid cells of  $\mathbf{T}$  traversed by the robot along  $\mathbf{s}_{1:N}$ .

2) *Goal distance cost ( $C_{\text{goal}}$ )*: By thresholding  $\mathbf{T}$ , we build a binary obstacle grid map  $\mathbf{O}$ . From  $\mathbf{O}$ , a geodesic distance field to the goal is derived [46]. Then  $C_{\text{goal}}$  is the sum of the geodesic distances of each waypoint to the goal, encouraging fast goal-reaching. When close to the goal, the heading difference  $|\theta_G - \theta_i|$  is added for goal alignment.

3) *Effort cost ( $C_{\text{effort}}$ )*: This is the weighted sum of the linear, lateral, and angular velocities  $w_{\text{lin}}|v^x| + w_{\text{lat}}|v^y| + w_{\text{ang}}|\omega|$  over the command sequence, encouraging efficient motion while discouraging unnecessary sideways motion and excessive turning.

### C. Dataset Curation

1) *Teleoperation Dataset ( $\mathcal{D}_{\text{TEL}}$ )*:  $\mathcal{D}_{\text{TEL}}$  consists of fixed-horizon, goal-conditioned segments extracted from the recorded teleoperated trajectories and serves to transfer semantic preferences and motion characteristics to the policy. Implementation details are provided in Appendix A1.

2) *Geometric Dataset ( $\mathcal{D}_{\text{GEO}}$ )*: To increase the diversity and scale of the training data, we employ the previously introduced MPPI-planner to generate additional demonstrations. For every camera frame  $\mathbf{I}$ , we independently sample  $K$  random goals  $\mathbf{g}_1, \dots, \mathbf{g}_K$  from a Gaussian distribution in the robot-centric coordinate frame (see Fig. 8 in the Appendix). Given the matching elevation map  $\mathbf{E}$  and the goals, MPPI plans the paths  $\mathbf{s}_{1:N}^1, \dots, \mathbf{s}_{1:N}^K$ ; generating  $K$  diverse training samples  $(\mathbf{I}, \mathbf{g}_i, \mathbf{s}_{1:N}^i)$  that are saved in  $\mathcal{D}_{\text{GEO}}$ .

The MPPI planner reliably generates geometrically feasible paths by leveraging privileged information from accurate elevation mapping. This enables the creation of demonstrations that are more diverse and exploratory than those obtained from real-world teleoperation alone. Even when a randomly sampled goal is infeasible, the planner still produces safe, embodiment-consistent behavior, either progressing toward the goal in a best-effort manner or exploring alternative routes while avoiding obstacles.

### D. Policy Architecture

$\pi$  receives a single RGB image  $\mathbf{I}$  together with a  $\text{SE}(2)$  goal  $\mathbf{g}$  in the robot-centric coordinate frame. It outputs  $N$  waypoints in  $\text{SE}(2)$ , also in the robot-centric frame.

First, a DINOv2 [47] image encoder is used to extract patch embeddings from the image  $\mathbf{I}$ . The goal pose  $\mathbf{g}$  is projected to the same embedding dimension and replicated  $N$  times. We call these  $N$  goal embeddings *waypoint queries*.

To every patch embedding and every waypoint query, we add an individually learned absolute positional embedding. Next, the *waypoint queries* are passed to a 4-block transformer decoder, with the patch embeddings used as keys and values.

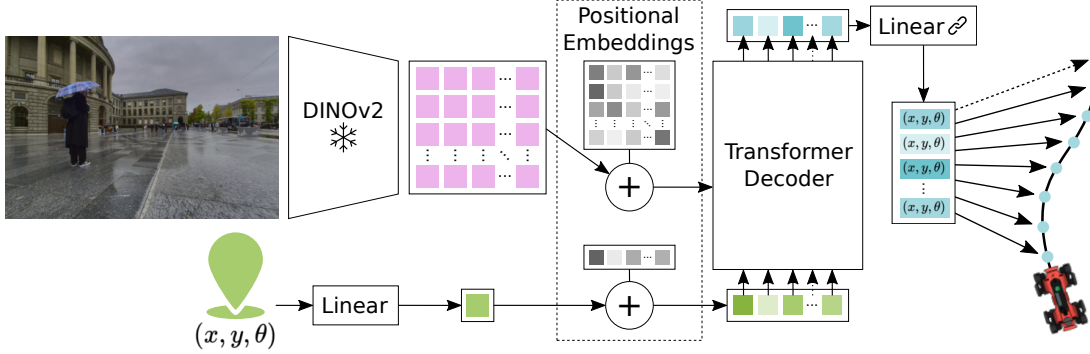


Fig. 3. Overview of LiMo’s architecture. The policy takes as input a single RGB image  $\mathbf{I}$ , and a goal pose  $\mathbf{g} = (x, y, \theta)$  in the robot-centric frame. Image features are extracted using a frozen DINOv2 encoder and combined with learned positional embeddings. A transformer decoder conditioned on the goal embedding predicts  $N$  waypoint embeddings, which are linearly projected to  $N$  waypoints  $(x, y, \theta)$ , forming the output trajectory.

The decoder outputs  $N$  *waypoint embeddings*, which are projected to  $N$  waypoints via a linear layer with weights shared across all positions. The resulting waypoint sequence forms the predicted plan. An overview of the architecture is shown in Fig. 3.

Further implementation details are available in Appendix A.

#### IV. EXPERIMENTS

In this section, we address the following questions: (Q1) Do the diverse geometric demonstrations effectively improve navigation performance? (Q2) Can LiMo generalize to unseen environments? (Q3) Does our method enable embodiment-specific navigation? (Q4) Does LiMo work when deployed on a real robot?

##### A. Datasets

The experiments build on the *GrandTour* dataset [1], which comprises 6 h of highly diverse deployments of an ANYmal D robot across 49 sites in Switzerland, with varying weather and lighting conditions. From these missions, we derive three datasets, in accordance with Secs. III-C1 and III-C2: (i) the teleoperation dataset  $\mathcal{D}_{\text{TEL}}$ , (ii) the geometric-planner-labeled dataset  $\mathcal{D}_{\text{GEO}}$  with  $K = 10$  trajectories per image, each with  $N = 50$  waypoints evenly spaced over  $T = 5$  s, and finally, (iii) the augmented dataset  $\mathcal{D}_{\text{AUG}} = \mathcal{D}_{\text{TEL}} \cup \mathcal{D}_{\text{GEO}}$ . For evaluation, we reserve six *GrandTour* missions exclusively as test scenes (see Tab III in the Appendix for further details on dataset size).

##### B. Qualitative Performance and Emergent Behavior

In Fig. 4, we present representative path predictions from LiMo. Examples (a, b, e, f, g, i, j, k) highlight a strong geometric understanding and embodiment-aware behavior: LiMo identifies door openings, plans to climb and descend stairs, and navigates rough natural terrain. Comparisons in column three (c, g, k) show that the  $\mathcal{D}_{\text{AUG}}$ -trained policy produces substantially more geometry-aware and obstacle-avoiding plans than the  $\mathcal{D}_{\text{TEL}}$ -only baseline, clearly indicating the benefit of including geometric demonstrations (Q1). The model also plans sensible trajectories in held-out missions (a,

d, g, j, k), demonstrating generalization to unseen environments (Q2), and consistently chooses behaviors aligned with ANYmal’s locomotion capabilities, confirming embodiment-specific navigation (Q3).

##### C. Quantitative Results

1) *Metrics*: Following the recommendations of [2], we evaluate trajectories on held-out missions using geodesic distances (GD) and *Success weighted by normalized inverse Path Length* (SPL). A path is deemed *successful* if (i) the GD, derived from the traversability map, of the final waypoint to the goal is  $\leq 1.0$  m and (ii) the robot does not collide. Let  $S_i \in \{0, 1\}$  indicate success for sample  $i$ ,  $\ell_i$  be the geodesic start-to-goal distance, and  $p_i$  the executed path length; then the SPL is defined as:

$$\text{SPL} = \frac{1}{N} \sum_{i=1}^N S_i \frac{\ell_i}{\max(p_i, \ell_i)}. \quad (5)$$

We evaluate only goals reachable by the geometric planner, to avoid penalizing methods for failing to reach inherently infeasible goals.

###### 2) *Baselines*:

a) *Straight line*: Paths go straight from the robot to the goals, capped at 5 m in length.

b) *Geometric planner*: The path obtained by running the planner described in Sec. III-B.

c) *OmniVLA (open-loop)* [35]: OmniVLA is a state-of-the-art visual navigation model initialized using the authors’ released checkpoint. Our benchmark measures open-loop, single-shot trajectory prediction for local goal-conditioned planning, whereas OmniVLA is primarily designed for closed-loop replanning. We therefore evaluate OmniVLA under this open-loop protocol, and the results should be interpreted accordingly.

3) *Results*: As shown in Tab II, incorporating geometric demonstrations yields substantial SPL improvements on the diverse  $\mathcal{D}_{\text{AUG}}$  test set, indicating that geometric supervision significantly strengthens performance in complex, unseen scenarios (Q1, Q2). As expected, when evaluating only on goals drawn from the  $\mathcal{D}_{\text{TEL}}$  distribution, the improvement is smaller.

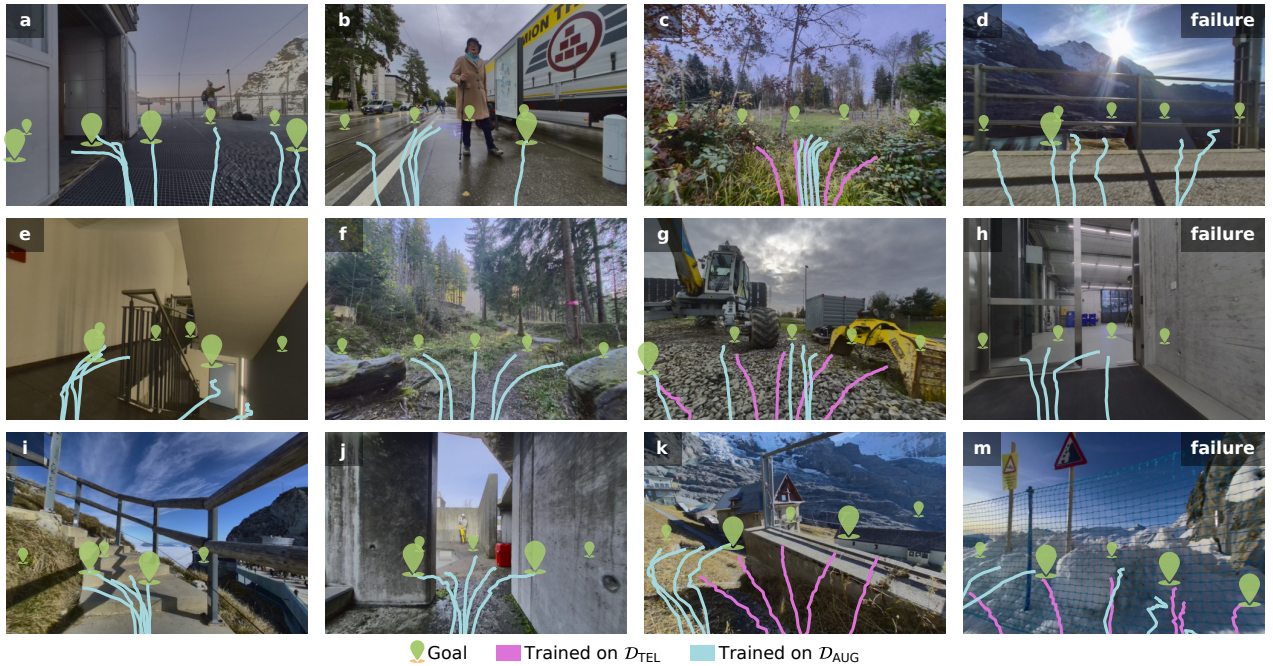


Fig. 4. Qualitative comparison of predicted trajectories across diverse indoor and outdoor scenarios. Images (b, c, e, f, h, i) are included in the training set, while (a, d, g, j, k, m) are held-out scenes. Column three compares predictions from the *teleop-only* policy with those from the *augmented-trained* policy, where the latter shows much better scene understanding. Column four illustrates the remaining failure cases. LiMO correctly recognizes door openings (a, j), handles stair ascent and descent consistent with ANYmal’s embodiment (e, i), and navigates unstructured natural terrain such as forests and fields (c, f). It also demonstrates robustness on construction sites (g) and in high-elevation outdoor environments (k), while remaining challenged by cliff edges (d), transparent surfaces, and obstacles such as glass doors and nets (h, m), and by unusual obstacles such as snow piles (m).

TABLE II  
EVALUATION SUMMARY SORTED BY SPL

Planner	Col. (%) ↓	Succ. (%) ↑	SPL (%) ↑
<b>Evaluated on <math>\mathcal{D}_{TEL}</math></b>			
<i>OmniVLA (open-loop)</i> [35]	12.6	67.2	41.5
Trained on $\mathcal{D}_{TEL}$	10.8	87.1	84.4
Trained on $\mathcal{D}_{AUG}$	11.1	88.7	86.4
<i>Straight line paths</i>	12.5	87.5	87.5
<i>Real world paths</i>	11.0	89.0	87.5
<i>Geometric planner</i>	3.7	96.3	88.8
<b>Evaluated on <math>\mathcal{D}_{AUG}</math></b>			
<i>OmniVLA (open-loop)</i> [35]	14.2	46.5	33.5
Trained on $\mathcal{D}_{TEL}$	14.1	51.4	49.7
<i>Straight line paths</i>	23.1	76.9	76.9
Trained on $\mathcal{D}_{AUG}$	14.5	82.2	80.0
<i>Geometric planner</i>	1.0	99.0	95.4

Since SPL explicitly rewards efficient, short paths, the *straight-line* baseline performs well on  $\mathcal{D}_{TEL}$ , where many goals lie roughly straight ahead, and few obstacles are encountered. This highlights that geometric augmentation is most beneficial in diverse, obstacle-rich scenarios, where simple straight-line behavior no longer suffices.

We observe that *OmniVLA* achieves competitive collision avoidance, even on the more challenging  $\mathcal{D}_{AUG}$  test set, but exhibits reduced goal-reaching performance under our open-loop evaluation. This behavior is expected in part due to the evaluation protocol: *OmniVLA* is trained for closed-loop

replanning with fixed-length waypoint chunks rather than open-loop trajectory termination at a specified goal.

In addition, we hypothesize that training on large, cross-embodiment datasets, dominated by wheeled platforms, can further limit goal-reaching accuracy for a specific embodiment, as the model must implicitly infer platform dynamics and feasible motions solely from visual context. Finally, the limited geometric diversity of legged-robot data within such datasets may restrict the model’s exposure to embodiment-specific maneuvers (e.g., lateral or in-place motions). A more detailed discussion of these factors is provided in Appendix B.

#### D. Ablations

1) *Training with fewer geometric paths per frame*: To explore the benefits of adding geometric paths, we train models on different mixtures of  $\mathcal{D}_{TEL}$  and  $\mathcal{D}_{GEO}$ . The policies are evaluated on the held-out test missions with  $\mathcal{D}_{TEL}$  or more diverse  $\mathcal{D}_{AUG}$  distributed goals. See Fig. 5 (left).

2) *Training on fewer missions*: To understand how well policies generalize when trained with fewer missions, we compare performance across varying numbers of training missions drawn from either  $\mathcal{D}_{TEL}$  or  $\mathcal{D}_{AUG}$ . Policies trained on a small number of diverse  $\mathcal{D}_{AUG}$  missions retain strong performance on  $\mathcal{D}_{TEL}$  goals, whereas policies trained only on  $\mathcal{D}_{TEL}$  require substantially more missions to reach comparable SPL (see Fig. 5 (Right)). This highlights that diversity in the training data, rather than sheer quantity, is key for efficient

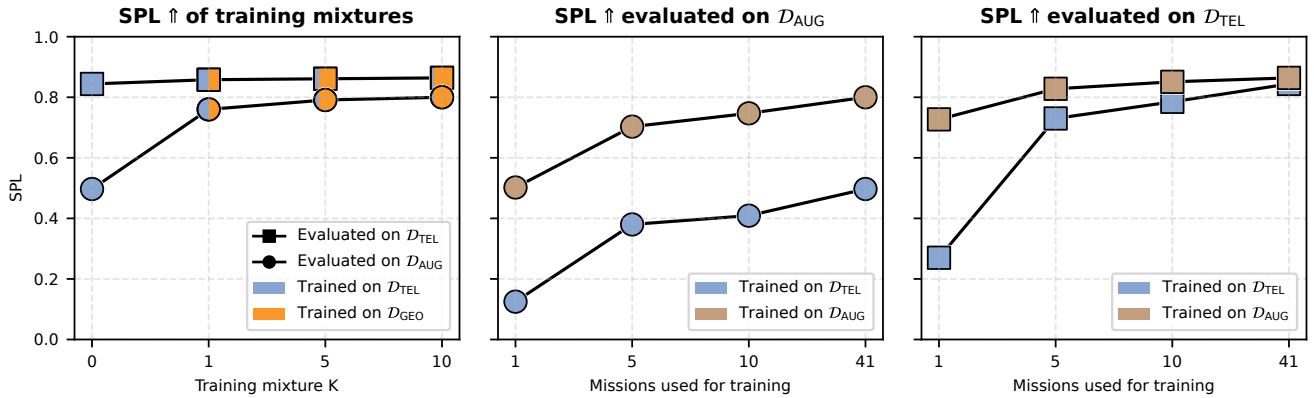


Fig. 5. (Left) Evaluation of SPL on  $D_{TEL}$  and  $D_{AUG}$  test sets trained on a varying number of augmenting geometric paths. Adding geometric samples mainly benefits performance on the more diverse  $D_{AUG}$  test split. (Middle) When evaluating goals following the  $D_{AUG}$  distribution, models trained solely on  $D_{TEL}$  consistently underperform compared to those trained on the  $D_{AUG}$ . While training on  $D_{AUG}$  generalizes well to  $D_{TEL}$ -style goals, models trained only on  $D_{TEL}$  fail to generalize to unseen diverse goals with limited data. (Right) Evaluation of SPL on  $D_{TEL}$  goals trained using the  $D_{TEL}$  and  $D_{AUG}$ . Training on just 5 missions of  $D_{AUG}$  achieves comparable performance to training on  $D_{TEL}$  with 41 missions.

generalization (Q1, Q2). Fig. 8 in the Appendix illustrates the difference in goal diversity among datasets.

#### E. Robot Deployment

We deploy LiMO in closed loop on an ANYmal D quadruped robot in locations outside the training scenes. These experiments aim to validate usability in real-world closed-loop control (Q4), embodiment-specific behavior (Q3), and robustness in unseen, cluttered environments (Q2). We showcase LiMO clearing obstacles, following corridors, and quickly reacting to dynamic scene changes.

We do not include on-robot comparisons to prior end-to-end visual navigation models. Existing approaches are designed for cross-embodiment deployment and often do not support pose-based goal conditioning. In contrast, LiMO predicts high-resolution, goal-pose-conditioned SE(2) trajectories that terminate at the commanded goal and are tailored to ANYmal’s embodiment. Moreover, representative models such as OmniVLA [35] are substantially larger, cannot be executed at comparable rates on the robot’s onboard hardware, and rely on additional mechanisms such as topological maps to provide subgoals. LiMO operates without such infrastructure.

Due to these fundamental differences in design objectives and deployment assumptions, real-robot comparisons are not directly interpretable and are therefore omitted.

1) *Deployment Setup*: We run LiMO on a NVIDIA Jetson Orin on-board the robot in closed loop at 6 Hz. We use a simple lookahead path follower node to make the robot track the predicted SE(2) waypoints. No geometric planning or sensing is used during the deployment. LiDAR point clouds are recorded solely to improve visualizations.

2) *Incorporating Side Cameras*: Using only the front-facing camera in closed-loop deployment led to collisions, as obstacles were no longer detected once they left the forward field of view. Therefore, in the robot experiments, we use a multi-camera variant with additional left- and right-facing cameras, implemented via a minimal architectural extension

that does not introduce memory or geometric sensing. A more detailed discussion of this limitation is given in Appendix C.

#### F. Obstacle Course Navigation

We design an indoor obstacle course comprising rigid obstacles and small traversable elements, requiring the robot to plan non-trivial paths while exploiting its legged mobility. The robot is given a single local goal and must navigate around obstacles without collisions (see Fig. 6). The experiment demonstrates that LiMO produces smooth, geometry-aware paths. Despite operating purely on vision at inference time, the predicted trajectories remain consistent with the robot’s footprint and motion capabilities.

#### G. Reacting to Dynamic Obstacles

To test reactivity, we introduce a moving obstacle by having a person carry a large mat and intentionally block the robot’s path during execution. The planner runs continuously at 6 Hz, allowing the robot to replan as the obstacle moves.

As shown in Fig. 7, the robot quickly deviates from its original path and selects alternative routes, including lateral and backward embodiment-specific motion, to avoid colliding. This behavior demonstrates that LiMO can handle dynamic environmental changes.

#### H. Corridor Following

We deploy the robot in a long corridor scenario with limited lateral clearance. The robot must stay centered as it progresses toward a goal located to the right of the corridor exit (see Fig. 10 in the Appendix).

## V. LIMITATIONS

Planner supervision depends on elevation and traversability estimates and can fail in edge cases, leading to unsafe or sub-optimal labels. At inference, LiMO operates on a single RGB frame without temporal memory, which limits reasoning under occlusions and causes obstacles to be forgotten once they leave the field of view. While geometric augmentation scales

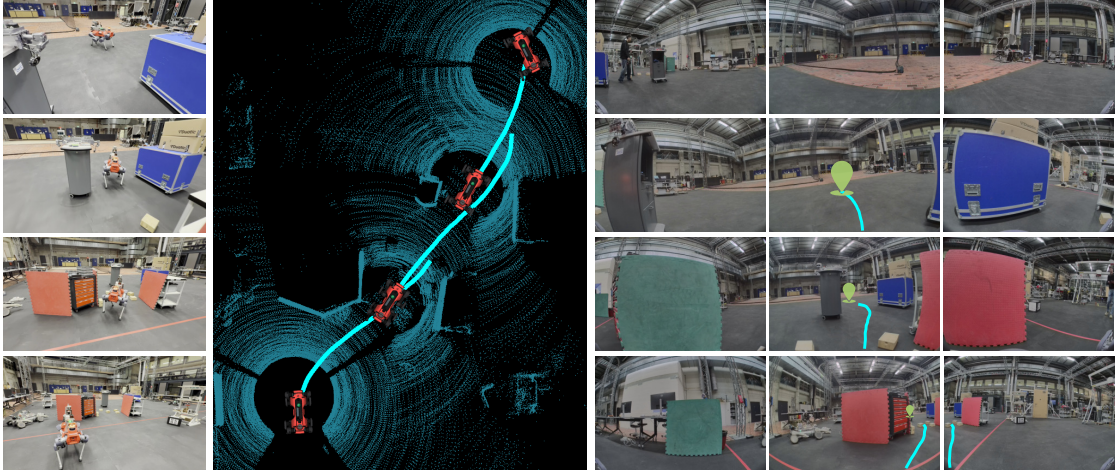


Fig. 6. Robot navigating an indoor obstacle course at four different time steps. From left to right: (i) third-person view, (ii) bird's-eye view of the LiDAR point cloud with predicted paths, and (iii) left-, front-, and right-facing camera views. The predicted trajectory is shown in cyan and the goal is shown in green. LiMO generates smooth, collision-free paths while adapting to obstacles.

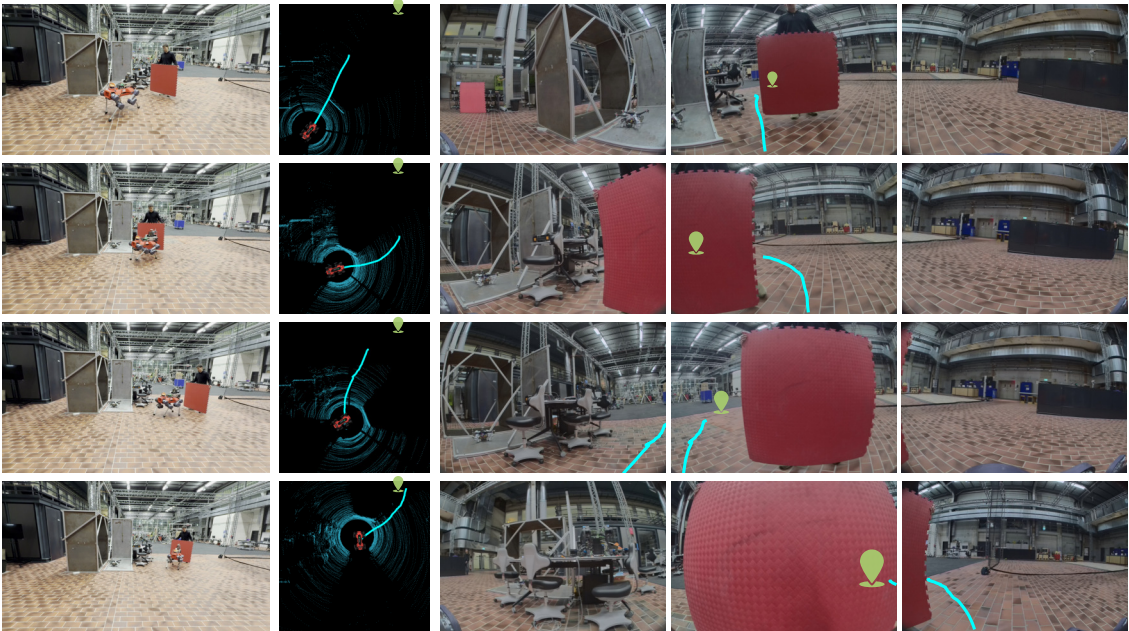


Fig. 7. The robot reacts to a dynamic obstacle (a person carrying a red mat). Rows show successive time steps during execution. From left to right: (i) third-person view, (ii) bird's-eye view of the LiDAR point cloud with predicted paths, and (iii) left-, front-, and right-facing camera views. The predicted trajectory (cyan) adapts online as the obstacle blocks the original path, leading to safe avoidance behavior.

supervision efficiently, visual diversity is still constrained by the underlying dataset. Fig. 4 illustrates representative failure cases, and a continued discussion is provided in Appendix D.

## VI. CONCLUSION

We presented LiMO, a goal-conditioned visual navigation policy trained on a mix of teleoperation data and scalable geometric supervision. By combining expert demonstrations with planner-generated trajectories that are fully embodiment-specific, we scale supervision to thousands of hours of high-quality trajectories. Across held-out missions, geometric augmentation leads to clear improvements in SPL, especially in

diverse, obstacle-rich environments. LiMO learns geometry-aware, semantically grounded behaviour aligned with ANYmal's embodiment, and experiments on a real robot validate its utility as a practical path planner.

Overall, our results show that for vision-based goal-conditioned navigation, curating diverse, geometry-aware supervision can be more effective than relying solely on large, heterogeneous datasets. By combining limited expert demonstrations with scalable, embodiment-specific geometric supervision, we provide a practical and data-efficient path toward robust visual navigation in real-world robotic systems.

## REFERENCES

[1] J. Frey, T. Tuna, L. F. T. Fu, C. Weibel, K. Patterson, B. Krummenacher, M. Müller, J. Nubert, M. Fallon, C. Cadena, and M. Hutter, "Boxi: Design Decisions in the Context of Algorithmic Performance for Robotics," in *Proceedings of Robotics: Science and Systems*, Los Angeles, United States, July 2025.

[2] P. Anderson, A. Chang, D. S. Chaplot, A. Dosovitskiy, S. Gupta, V. Koltun, J. Kosecka, J. Malik, R. Mottaghi, M. Savva, and A. R. Zamir, "On evaluation of embodied navigation agents," 2018. [Online]. Available: <https://arxiv.org/abs/1807.06757>

[3] P. Fankhauser, M. Bloesch, and M. Hutter, "Probabilistic terrain mapping for mobile robots with uncertain localization," *IEEE Robotics and Automation Letters*, vol. 3, no. 4, pp. 3019–3026, 2018.

[4] P. E. Hart, N. J. Nilsson, and B. Raphael, "A formal basis for the heuristic determination of minimum cost paths," *IEEE Transactions on Systems Science and Cybernetics*, vol. 4, no. 2, pp. 100–107, 1968.

[5] G. Williams, P. Drews, B. Goldfain, J. M. Rehg, and E. A. Theodorou, "Aggressive driving with model predictive path integral control," in *2016 IEEE International Conference on Robotics and Automation (ICRA)*. IEEE Press, 2016, p. 1433–1440. [Online]. Available: <https://doi.org/10.1109/ICRA.2016.7487277>

[6] C. Pinneri, S. Sawant, S. Blaes, J. Achterhold, J. Stueckler, M. Rolinek, and G. Martius, "Sample-efficient cross-entropy method for real-time planning," in *Conference on Robot Learning 2020*, 2020. [Online]. Available: [https://corlconf.github.io/paper\\_217](https://corlconf.github.io/paper_217)

[7] P. Papadakis, "Terrain traversability analysis methods for unmanned ground vehicles: A survey," *Engineering Applications of Artificial Intelligence*, vol. 26, no. 4, pp. 1373–1385, 2013. [Online]. Available: <https://www.sciencedirect.com/science/article/pii/S095219761300016X>

[8] J. Frey, M. Mattamala, N. Chebrolu, C. Cadena, M. Fallon, and M. Hutter, "Fast Traversability Estimation for Wild Visual Navigation," in *Proceedings of Robotics: Science and Systems*, Daegu, Republic of Korea, July 2023.

[9] Y. Zhu, R. Mottaghi, E. Kolve, J. J. Lim, A. Gupta, L. Fei-Fei, and A. Farhadi, "Target-driven visual navigation in indoor scenes using deep reinforcement learning," in *2017 IEEE International Conference on Robotics and Automation (ICRA)*. IEEE Press, 2017, p. 3357–3364. [Online]. Available: <https://doi.org/10.1109/ICRA.2017.7989381>

[10] P. Mirowski, R. Pascanu, F. Viola, H. Soyer, A. Ballard, A. Banino, M. Denil, R. Goroshin, L. Sifre, K. Kavukcuoglu, D. Kumaran, and R. Hadsell, "Learning to navigate in complex environments," in *International Conference on Learning Representations*, 2017. [Online]. Available: <https://openreview.net/forum?id=SJMGPrle>

[11] S. Gupta, V. Tolani, J. Davidson, S. Levine, R. Sukthankar, and J. Malik, "Cognitive mapping and planning for visual navigation," *Int. J. Comput. Vision*, vol. 128, no. 5, p. 1311–1330, May 2020. [Online]. Available: <https://doi.org/10.1007/s11263-019-01236-7>

[12] A. Loquercio, A. I. Maqueda, C. R. del Blanco, and D. Scaramuzza, "Dronet: Learning to fly by driving," *IEEE Robotics and Automation Letters*, vol. 3, no. 2, pp. 1088–1095, 2018.

[13] L. Le Mero, D. Yi, M. Dianati, and A. Mouzakitis, "A survey on imitation learning techniques for end-to-end autonomous vehicles," *IEEE Transactions on Intelligent Transportation Systems*, vol. 23, no. 9, pp. 14 128–14 147, 2022.

[14] H. M. Eraqi, M. N. Moustafa, and J. Honer, "Dynamic conditional imitation learning for autonomous driving," *IEEE Transactions on Intelligent Transportation Systems*, vol. 23, no. 12, pp. 22 988–23 001, 2022.

[15] B. Liao, S. Chen, H. Yin, B. Jiang, C. Wang, S. Yan, X. Zhang, X. Li, Y. Zhang, Q. Zhang, and X. Wang, "Diffusiondrive: Truncated diffusion model for end-to-end autonomous driving," *arXiv preprint arXiv:2411.15139*, 2024.

[16] NVIDIA, Y. Wang, W. Luo, J. Bai, Y. Cao, T. Che, K. Chen, Y. Chen, J. Diamond, Y. Ding, W. Ding, L. Feng, G. Heinrich, J. Huang, P. Karkus, B. Li, P. Li, T.-Y. Lin, D. Liu, M.-Y. Liu, L. Liu, Z. Liu, J. Lu, Y. Mao, P. Molchanov, L. Pavao, Z. Peng, M. Ranzinger, E. Schmerling, S. Shen, Y. Shi, S. Tariq, R. Tian, T. Wekel, X. Weng, T. Xiao, E. Yang, X. Yang, Y. You, X. Zeng, W. Zhang, B. Ivanovic, and M. Pavone, "Alpamayo-r1: Bridging reasoning and action prediction for generalizable autonomous driving in the long tail," 2026. [Online]. Available: <https://arxiv.org/abs/2511.00088>

[17] F. Yu, H. Chen, X. Wang, W. Xian, Y. Chen, F. Liu, V. Madhavan, and T. Darrell, "Bdd100k: A diverse driving dataset for heterogeneous multitask learning," 2020. [Online]. Available: <https://arxiv.org/abs/1805.04687>

[18] P. Sun, H. Kretzschmar, X. Dotiwalla, A. Chouard, V. Patnaik, P. Tsui, J. Guo, Y. Zhou, Y. Chai, B. Caine, V. Vasudevan, W. Han, J. Ngiam, H. Zhao, A. Timofeev, S. Ettinger, M. Krivokon, A. Gao, A. Joshi, Y. Zhang, J. Shlens, Z. Chen, and D. Anguelov, "Scalability in perception for autonomous driving: Waymo open dataset," in *2020 IEEE/CVF Conference on Computer Vision and Pattern Recognition (CVPR)*, 2020, pp. 2443–2451.

[19] K. T. e. a. H. Caesar, J. Kabzan, "Nuplan: A closed-loop ml-based planning benchmark for autonomous vehicles," in *CVPR ADP3 workshop*, 2021.

[20] D. Shah, A. Sridhar, N. Dashora, K. Stachowicz, K. Black, N. Hirose, and S. Levine, "ViNT: A foundation model for visual navigation," *7th Annual Conference on Robot Learning*, 2023. [Online]. Available: <https://arxiv.org/abs/2306.14846>

[21] A. Sridhar, D. Shah, C. Glossop, and S. Levine, "NoMaD: Goal Masked Diffusion Policies for Navigation and Exploration," *IEEE International Conference on Robotics and Automation (ICRA)*, 2024. [Online]. Available: <https://arxiv.org/abs/2310.07896>

[22] S. Gode, A. Nayak, D. N. Oliveira, M. Krawez, C. Schmid, and W. Burgard, "Flownav: Combining flow matching and depth priors for efficient navigation," 2025. [Online]. Available: <https://arxiv.org/abs/2411.09524>

[23] D. Shah and S. Levine, "ViKiNG: Vision-Based Kilometer-Scale Navigation with Geographic Hints," in *Proceedings of Robotics: Science and Systems*, 2022. [Online]. Available: <http://www.robotsproceedings.org/rss18/p019.html>

[24] G. Kahn, A. Villaflor, B. Ding, P. Abbeel, and S. Levine, "Self-supervised deep reinforcement learning with generalized computation graphs for robot navigation," in *2018 IEEE International Conference on Robotics and Automation (ICRA)*. IEEE Press, 2018, p. 1–8. [Online]. Available: <https://doi.org/10.1109/ICRA.2018.8460655>

[25] N. Hirose, F. Xia, R. Martín-Martín, A. Sadeghian, and S. Savarese, "Deep visual mpc-policy learning for navigation," *IEEE Robotics and Automation Letters*, vol. 4, no. 4, pp. 3184–3191, 2019.

[26] A. Agha *et al.*, "Nebula: Quest for robotic autonomy in challenging environments; team costar at the darpa subterranean challenge," 2021. [Online]. Available: <https://arxiv.org/abs/2103.11470>

[27] D. Shah, B. Eysenbach, N. Rhinehart, and S. Levine, "Rapid exploration for open-world navigation with latent goal models," in *Proceedings of the 5th Conference on Robot Learning*, ser. Proceedings of Machine Learning Research, A. Faust, D. Hsu, and G. Neumann, Eds., vol. 164. PMLR, 08–11 Nov 2022, pp. 674–684. [Online]. Available: <https://proceedings.mlr.press/v164/shah22a.html>

[28] N. Hirose, D. Shah, A. Sridhar, and S. Levine, "Sacson: Scalable autonomous control for social navigation," *IEEE Robotics and Automation Letters*, vol. 9, no. 1, pp. 49–56, 2024.

[29] H. Karnan, A. Nair, X. Xiao, G. Warnell, S. Pirk, A. Toshev, J. Hart, J. Biswas, and P. Stone, "Socially compliant navigation dataset (scand): A large-scale dataset of demonstrations for social navigation," *IEEE Robotics and Automation Letters*, 2022.

[30] A. Shaban, X. Meng, J. Lee, B. Boots, and D. Fox, "Semantic terrain classification for off-road autonomous driving," in *Proceedings of the 5th Conference on Robot Learning*, ser. Proceedings of Machine Learning Research, A. Faust, D. Hsu, and G. Neumann, Eds., vol. 164. PMLR, 08–11 Nov 2022, pp. 619–629. [Online]. Available: <https://proceedings.mlr.press/v164/shaban22a.html>

[31] S. Triest, M. Sivaprakasam, S. J. Wang, W. Wang, A. M. Johnson, and S. Scherer, "Tartandrive: A large-scale dataset for learning off-road dynamics models," in *2022 International Conference on Robotics and Automation (ICRA)*. IEEE Press, 2022, p. 2546–2552. [Online]. Available: <https://doi.org/10.1109/ICRA46639.2022.9811648>

[32] N. Hirose, C. Glossop, A. Sridhar, D. Shah, O. Mees, and S. Levine, "Lelan: Learning a language-conditioned navigation policy from in-the-wild video," in *Conference on Robot Learning*, 2024.

[33] X. Liu, J. Li, Y. Jiang, N. Sujay, Z. Yang, J. Zhang, J. Abanes, J. Zhang, and C. Feng, "Citywalker: Learning embodied urban navigation from web-scale videos," in *Proceedings of the Computer Vision and Pattern Recognition Conference*, 2025, pp. 6875–6885.

[34] N. Hirose, L. Ignatova, K. Stachowicz, C. Glossop, S. Levine, and D. Shah, "Learning to drive anywhere with model-based reannotation," 2025. [Online]. Available: <https://arxiv.org/abs/2505.05592>

[35] N. Hirose, C. Glossop, D. Shah, and S. Levine, "Omnivila: An omni-modal vision-language-action model for robot navigation," 09 2025.

[36] M. Patel, F. Yang, Y. Qiu, C. Cadena, S. Scherer, M. Hutter, and W. Wang, “Tartanground: A large-scale dataset for ground robot perception and navigation,” in *2025 IEEE/RSJ International Conference on Intelligent Robots and Systems (IROS)*, 2025, pp. 20524–20531.

[37] K. Stachowicz, L. Ignatova, and S. Levine, “Lifelong autonomous improvement of navigation foundation models in the wild,” in *8th Annual Conference on Robot Learning*, 2024. [Online]. Available: <https://openreview.net/forum?id=vBj5oC60Lk>

[38] A.-C. Cheng, Y. Ji, Z. Yang, X. Zou, J. Kautz, E. Biyik, H. Yin, S. Liu, and X. Wang, “Navila: Legged robot vision-language-action model for navigation,” in *RSS*, 2025.

[39] M. J. Kim, K. Pertsch, S. Karamcheti, T. Xiao, A. Balakrishna, S. Nair, R. Rafailov, E. P. Foster, P. R. Sanketi, Q. Vuong, T. Kollar, B. Burchfiel, R. Tedrake, D. Sadigh, S. Levine, P. Liang, and C. Finn, “OpenVLA: An open-source vision-language-action model,” in *Proceedings of The 8th Conference on Robot Learning*, ser. Proceedings of Machine Learning Research, P. Agrawal, O. Kroemer, and W. Burgard, Eds., vol. 270. PMLR, 06–09 Nov 2025, pp. 2679–2713. [Online]. Available: <https://proceedings.mlr.press/v270/kim25c.html>

[40] H. Xu, Y. Gao, F. Yu, and T. Darrell, “End-to-End Learning of Driving Models from Large-Scale Video Datasets,” in *2017 IEEE Conference on Computer Vision and Pattern Recognition (CVPR)*. Los Alamitos, CA, USA: IEEE Computer Society, Jul. 2017, pp. 3530–3538. [Online]. Available: <https://doi.ieeecomputersociety.org/10.1109/CVPR.2017.376>

[41] A. Zhang, X. Meng, L. Calliari, D.-K. Kim, S. Omidshafiei, J. Biswas, A. Agha, and A. Shaban, “Ventura: Adapting image diffusion models for unified task conditioned navigation,” 2025. [Online]. Available: <https://arxiv.org/abs/2510.01388>

[42] J. Peng, W. Cai, Y. Yang, T. Wang, Y. Shen, and J. Pang, “Logoplanner: Localization grounded navigation policy with metric-aware visual geometry,” 2025.

[43] J. Alvarez-Padilla, J. Z. Zhang, S. Kwok, J. M. Dolan, and Z. Manchester, “Real-time whole-body control of legged robots with model-predictive path integral control,” in *2025 IEEE International Conference on Robotics and Automation (ICRA)*. IEEE, 2025, pp. 14721–14727.

[44] T. Miki, L. Wellhausen, R. Grandia, F. Jenelten, T. Homberger, and M. Hutter, “Elevation mapping for locomotion and navigation using gpu,” in *2022 IEEE/RSJ International Conference on Intelligent Robots and Systems (IROS)*. IEEE, 2022, pp. 2273–2280.

[45] G. Erni, J. Frey, T. Miki, M. Mattamala, and M. Hutter, “Mem: Multi-modal elevation mapping for robotics and learning,” in *2023 IEEE/RSJ International Conference on Intelligent Robots and Systems (IROS)*. IEEE, 2023, pp. 11011–11018.

[46] M. Asad, R. Dorent, and T. Vercauteren, “Fastgeodis: Fast generalised geodesic distance transform,” *Journal of Open Source Software*, vol. 7, no. 79, p. 4532, 2022. [Online]. Available: <https://doi.org/10.21105/joss.04532>

[47] M. Oquab, T. Darzet, T. Moutakanni, H. V. Vo, M. Szafraniec, V. Khalidov, P. Fernandez, D. HAZIZA, F. Massa, A. El-Nouby, M. Assran, N. Ballas, W. Galuba, R. Howes, P.-Y. Huang, S.-W. Li, I. Misra, M. Rabbat, V. Sharma, G. Synnaeve, H. Xu, H. Jegou, J. Mairal, P. Labatut, A. Joulin, and P. Bojanowski, “DINOv2: Learning robust visual features without supervision,” *Transactions on Machine Learning Research*, 2024, featured Certification. [Online]. Available: <https://openreview.net/forum?id=a68SU16zFt>

[48] I. Loshchilov and F. Hutter, “Decoupled weight decay regularization,” in *International Conference on Learning Representations*, 2017. [Online]. Available: <https://api.semanticscholar.org/CorpusID:53592270>

[49] L. N. Smith and N. Topin, “Super-convergence: very fast training of neural networks using large learning rates,” in *Artificial Intelligence and Machine Learning for Multi-Domain Operations Applications*, T. Pham, Ed., vol. 11006, International Society for Optics and Photonics. SPIE, 2019, p. 1100612. [Online]. Available: <https://doi.org/10.1117/12.2520589>

[50] J. Wang, M. Chen, N. Karaev, A. Vedaldi, C. Rupprecht, and D. Novotny, “Vggt: Visual geometry grounded transformer,” in *Proceedings of the IEEE/CVF Conference on Computer Vision and Pattern Recognition*, 2025.

## APPENDIX

### A. Implementation Details

1) *Teleoperation Dataset* ( $\mathcal{D}_{TEL}$ ): We extract goal-conditioned training samples from  $\mathcal{D}_{Base}$ , which provides time-synchronized images and state estimates from teleoperated missions. Let  $\bar{s}(t) \in \text{SE}(2)$  denote the recorded robot pose at time  $t$ . For each camera frame at time  $t_0$  with image  $\mathbf{I}(t_0)$ , we sample a future time  $t_g > t_0$  and set the goal to the corresponding future pose, expressed in the robot-centric frame at  $t_0$ .

We construct a fixed-horizon waypoint sequence of length  $N$  with step size  $\Delta t$  (horizon  $T = N\Delta t$ ) by sampling poses from the teleoperation trajectory. We uniformly sample  $N$  timestamps over the interval  $[t_0, t_0 + \min(T, t_g - t_0)]$  and set each waypoint to the recorded pose at that timestamp, i.e.,  $\mathbf{s}_i = \bar{s}(t_i)$ . If  $t_g - t_0 > T$ , the segment covers the next  $T$  seconds of teleoperation and typically does not reach the goal. If  $t_g - t_0 \leq T$ , we time-warp the segment by sampling the full interval  $[t_0, t_g]$  into  $N$  waypoints, ensuring a fixed output horizon and smoothing abrupt stops near the goal. Each sample is stored as  $(\mathbf{I}, \mathbf{g}, \mathbf{s}_{1:N})$  in  $\mathcal{D}_{TEL}$ .

2) *Traversability Mapping*: The CNN output is classified into different regions. Cells with  $< 0.3$  are classified as safe and assigned a traversability cost of 0. Between 0.3 and 0.8, we use a linear ramp to map to traversability costs. Cells above 0.8 are deemed risky and assigned a cost of 2.0. Anything above 0.9 is an obstacle and is assigned a cost of  $10^5$ .

3) *Goal Sampling*: For each frame, we draw  $K$  goals from  $\mathcal{N}([5 \text{ m}, 0 \text{ m}, 0]^\top, \text{diag}(2.5^2 \text{ m}, 2.0^2 \text{ m}, (\pi/4)^2))$  (Fig. 8).

4) *Rollouts and Footprint*: MPPI uses horizon  $T = 50$  with  $\Delta t = 0.1 \text{ s}$ . The robot footprint (dilated by a safety margin) is rasterized on the grid for collision queries along rollouts.

5) *Dataset Filtering*: We discard stationary or near-stationary segments with a final displacement  $< 0.25 \text{ m}$  to reduce redundancy in  $\mathcal{D}_{TEL}$ . In  $\mathcal{D}_{GEO}$ , we discard frames in which the elevation map contains fewer than 25% valid measurements.

6) *Gridmaps*: The traversability and GDF are represented as  $8 \times 8 \text{ m}$  grid maps with a  $4 \times 4 \text{ cm}$  resolution, centered around the robot.

7) *Architecture*: Our policy consists of a frozen DINOv2 ViT-S/14 image encoder and a lightweight transformer decoder for waypoint prediction. All DINOv2 parameters are frozen except for LayerNorm layers. The full model contains approximately 32 M parameters, of which 10 M are trainable.

8) *Training*: We train LiMO using standard supervised regression with an L2-loss on the predicted waypoints and train for 16 epochs using AdamW [48] with a OneCycleLR [49] schedule. This equates to 1.4 M steps with a batch size of 16 on a single NVIDIA RTX-4090 GPU. Longer training did not further improve performance.

### B. OmniVLA Comparison

OmniVLA [35] is a visual navigation model that supports multiple goal-conditioning modalities (SE(2) goal pose, goal

image, language instructions, and their combinations) and predicts short-horizon navigation commands. In the released inference code, OmniVLA outputs a sequence of 8 future “actions,” corresponding to *relative waypoints* (consistent with the ViNT [20] and NoMaD [21] representation) that are tracked by a low-level controller.

OmniVLA is trained to imitate a fixed-length chunk of 8 waypoints, even when the provided goal lies within this horizon. According to the authors (email communication), the goal pose is treated as one of several subgoals along a trajectory, and the model is trained to predict the full waypoint chunk, regardless of whether the goal is reached before step 8.

As a result, OmniVLA is not explicitly trained to produce trajectories that terminate at the goal in open loop; instead, stopping behavior is handled by the downstream waypoint tracker.

a) *Evaluation Protocol*: We evaluate OmniVLA in pose-only conditioning mode using the released checkpoints. To enable a fair comparison in open-loop evaluation, we report success if the *closest* waypoint in the predicted sequence is within 1 m of the goal, rather than requiring the final waypoint to coincide with it. Predicted waypoints are de-normalized using the scaling constant (metric\_waypoint\_spacing) as in the official code, chosen to match the scale of our local planning horizon.

b) *Model Scale and Motion Diversity*: OmniVLA’s support of broad conditioning modalities comes at the cost of high model complexity and size. It builds on OpenVLA [39], a 7 B-parameter vision-language-action model pretrained primarily for manipulation. OmniVLA uses pretraining from OpenVLA and is further adapted for navigation using a cross-embodiment dataset heavily dominated by wheeled platforms (e.g., BDD-V [40], Frolobots-2K [34]). Consequently, OmniVLA produces paths that are almost exclusively forward-moving, and conditioning signals predominantly modulate steering rather than enabling diverse motion behaviors.

In contrast, LiMO is a lightweight model with 32 M parameters (10 M trainable), trained for embodiment-specific navigation. It predicts 50 waypoints, providing finer temporal resolution and longer horizon planning. Its training data includes sideways, backward, and in-place motions characteristic of legged locomotion, enabling full SE(2) planning consistent with quadruped behavior.

c) *Discussion*: Under this protocol, OmniVLA exhibits competitive collision avoidance but substantially lower goal-reaching performance than LiMO on our evaluation (Tab II). We attribute this primarily to OmniVLA’s closed-loop training assumptions and the strong bias toward wheeled-platform motion in its training data.

Moreover, OmniVLA is trained as a cross-embodiment policy without explicit knowledge of the target robot’s physical characteristics and therefore lacks an internal notion of the platform’s size and maneuverability. This absence of embodiment awareness hinders precise goal-reaching, particularly for a legged robot whose motion capabilities differ substantially from the car-like behaviors.

Whereas LiMO’s training is explicitly tailored to ANYmal’s geometry and traversability model, enabling more accurate and platform-consistent planning.

Overall, this comparison suggests that simply scaling navigation policies to large, heterogeneous datasets does not necessarily yield robust, accurate, goal-conditioned planning. This raises the broader question of whether embodiment-agnostic foundation models are sufficient for robotic navigation, or whether effective navigation requires supervision grounded in the geometry and constraints of the target robot.

### C. Incorporating Side Cameras

When relying solely on the front-facing camera, LiMO cannot maintain awareness of obstacles once they leave the field of view. This can lead to collisions when the policy corrects the robot’s path before fully clearing an obstacle.

Incorporating explicit memory or leveraging past observations could mitigate this issue, but we consider such extensions orthogonal to the focus of this work and leave them for future research. Instead, we addressed the issue by adding the robots’ left- and right-facing camera views to the training data and by minimally modifying the policy architecture to also use the side cameras.

Image features are extracted using the same shared DINOv2 encoder from all three camera views. The features are enriched with an additional learned absolute positional embedding, allowing the decoder to differentiate between features from different camera views. All image features are forwarded to the decoder; otherwise, it remains unchanged. This way, LiMO can still register obstacles to the side, even after mostly clearing them. Fig. 9 compares predictions of the policy with and without side camera views.

This limitation is less critical for cross-embodiment models such as OmniVLA, whose training on predominantly wheeled platforms induces conservative, Ackermann-like behavior. Because these models mainly adjust steering while moving forward, they rarely make early lateral corrections that provoke collisions when obstacles exit the forward field of view.

LiMO, in contrast, deliberately exploits more agile motion capabilities of quadruped robots, making it more sensitive to this effect and motivating the use of side-camera observations.

### D. Limitations

Our method inherits limitations from the geometric supervisor. The MPPI planner depends on elevation and traversability estimates that can fail in edge cases; for example, cliff edges may be classified as safe (Fig. 4-d), and difficult terrain can lead to suboptimal geometric paths.

While expert demonstrations provide semantic cues, they are limited in scale, so LiMO may still struggle when semantics play a critical role. Also, simply combining the datasets sample by sample might not be the optimal way to convey semantic and geometric cues. A mechanism for selectively choosing or weighting samples during training could be promising.

We can scale the amount of supervision, but the visual diversity of the dataset’s scenes remains fixed. Pretrained

encoders, such as DINOv2 [47], help; yet out-of-distribution cases, for example, the net and snow in Fig. 4-m, remain challenging.

Finally, LiMO operates on a single RGB frame without temporal memory, which limits its ability to handle occlusions or reason over longer time horizons. This can lead to LiMO forgetting obstacles when they leave the field of view, or to oscillations or temporally inconsistent plans.

### E. Future Work

Several extensions could further improve performance and scalability. (i) Following Alpamayo-R1 [16], direct waypoint regression could be replaced with a discretized trajectory representation and a generative objective such as conditional flow matching, which may better capture the inherently multimodal distribution of feasible paths in ambiguous scenes.

(ii) Our geometric supervision currently relies on co-registered elevation maps; leveraging camera-only datasets by extracting scene geometry using pretrained models such as VGGT [50] could broaden the training distribution.

(iii) More principled strategies for sampling or weighting expert versus planner supervision may improve the transfer of semantic preferences while preserving strong geometric safety.

(iv) Incorporating temporal context is another promising direction: memory-based approaches could maintain awareness of previously observed obstacles without requiring additional cameras.

### ACKNOWLEDGMENTS

The authors would like to thank Turcan Tuna and William Talbot for their support during robot experiments and system integration. We also thank members of the Robotic Systems Lab at ETH Zurich for valuable discussions and feedback throughout the project. We thank the authors of OmniVLA for providing model checkpoints, code snippets, and helpful clarifications.

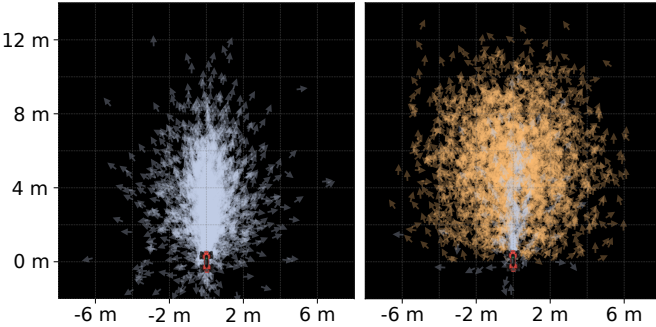


Fig. 8. Visualization of goal distributions based on 10,000 samples from each dataset. (Left) Goals from the teleoperation dataset  $\mathcal{D}_{\text{TEL}}$  (blue), sampled along the teleoperated trajectories. (Right) Goals from the augmented dataset  $\mathcal{D}_{\text{AUG}}$ , including teleoperation goals (blue) and additional randomly sampled goals (orange).

TABLE III  
DATASET STATISTICS

Dataset	Split	#Samples	Length [m]	Time [h]	Avg. vel. [m/s]
$\mathcal{D}_{\text{TEL}}$	Train	113 326	281 870	157	0.50
	Test	17 139	43 212	24	0.50
$\mathcal{D}_{\text{GEO}}$	Train	1 289 930	4 457 729	1792	0.69
	Test	191 060	653 978	265	0.68
$\mathcal{D}_{\text{AUG}}$	Train	1 403 256	4 739 599	1949	0.68
	Test	208 199	697 190	289	0.67

Each sample is a fixed-horizon waypoint sequence with duration  $T = 5$  s. The reported path length is the sum of Euclidean distances between consecutive waypoints. The reported average velocity should be interpreted with care: while the robot typically walks at around 1 m/s, many samples include stopping behavior (e.g., trajectories that reach the goal early), which lowers the mean speed.

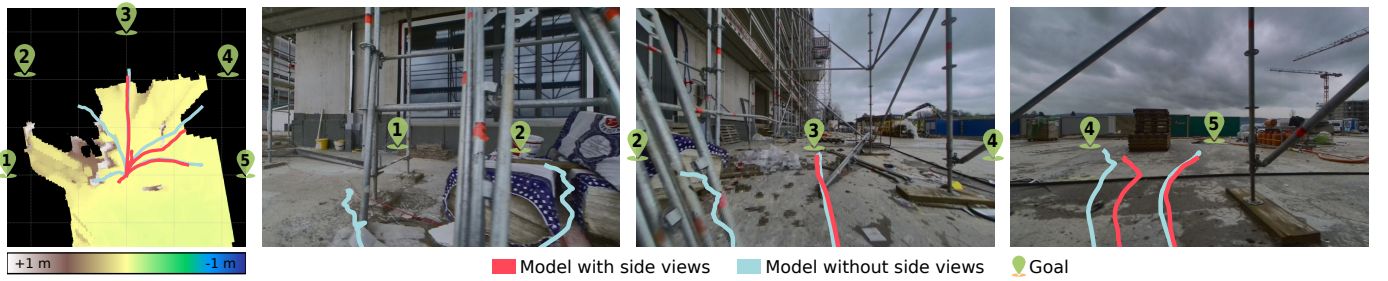


Fig. 9. Comparison of trajectory predictions with and without side-facing cameras. Five goals (green) and the corresponding predicted trajectories are shown. Using only the front camera (cyan), LiMO loses awareness of a partially cleared obstacle once it leaves the forward field of view, leading to collisions. With left and right side camera views (red), obstacle awareness is preserved, and all paths remain collision-free.



Fig. 10. The robot is following a narrow corridor toward a goal located at the far end. From left to right: (i) third-person view, (ii) bird's-eye view of the LiDAR point cloud with predicted paths, and (iii) left-, front-, and right-facing camera views. The predicted trajectory (cyan) remains centered and collision-free despite tight lateral constraints.